CrossMark

Electrochemistry of Nanocrystalline $La_{0.5}Sr_{0.5}MnO_3$ Perovskite for the Oxygen Reduction Reaction in Alkaline Medium

Noureddine Khellaf[1,2] · Abdelkrim Kahoul[2] · Farid Naamoune[2] · Nicolas Alonso-Vante[1]

Abstract Nanocrystalline $La_{0.5}Sr_{0.5}MnO_3$ (LSMO) perovskite-sized powders were successfully synthesized at heating low temperature and time using the Pechini method based on polyesterification between citric acid and ethylene glycol. The electroactivity of carbon-supported perovskite (LSMO/C) for the oxygen reduction reaction (ORR) was evaluated. The results showed that the electroactivity of LSMO/C largely depends on the calcination temperature, type of electrolyte, and mass loading. It increased remarkably with the calcination temperature in 0.1 M KOH. The ORR performance was examined in KOH, NaOH, and K_2SO_4. Higher electroactivity was recorded in KOH electrolyte, as compared to NaOH and K_2SO_4.

Keywords Nanoparticles · Pechini method · Perovskite · Oxygen reduction · Alkaline medium

Introduction

The oxygen reduction reaction (ORR) has been studied at length due to its great importance in energy conversion and storage devices and extended to alkaline fuel cells [1], electrolyzers [2], and metal-air batteries [3]. In alkaline media, the ORR proceeds as in the acid counter-part, either via two-electron $O_2+H_2O + 2e^-\rightarrow HO_2^-+OH^-$ or four-electron $O_2+2H_2O + 4e^-\rightarrow 4OH^-$ pathways. Many researchers are doing their best to find suitable electrocatalysts that could support the desired four-electron reduction process leading to an efficient energy conversion [4]. Although noble metals are suitable ones and have proved to be effective oxygen electrodes, the high costs and scarcity prevent their large-scale application. In order to reduce these costs, alternative non-precious metal oxides with comparable ORR activity to Pt-based catalysts are highly desirable for the development of fuel cells. In this regard, oxides with perovskite structure (ABO_3) have received wide attention due to their high activity and stability when used in alkaline media [5]. For instance, it has been reported that $LaMnO_3$ showed the best catalytic activity for both ORR and oxygen evolution reaction (OER) in 6 M KOH, whereas the $LaCoO_3$ showed the best stability [6]. Recently, considerable attention has been paid to strontium doped-perovskite materials, e.g., $La_{1-x}Sr_xMnO_3$ (LSMO) as cathode catalysts. These materials are broadly established as ORR/OER bifunctional electrode materials. The particle size and microstructure are significant for the electrodes' performance [5, 7]. As one of the most frequently used oxygen electrodes of alkaline [7] and oxide [8] fuel cells, $La_{0.5}Sr_{0.5}MnO_3$ (LSMO) perovskite oxide has proved promising catalytic properties [8]. Although this perovskite oxide, mentioned above, has provided interesting electrocatalytic properties in fuel cells, the literature however reports, to the best of our knowledge, few studies about the effect of the preparation method using low-temperature synthesis during a short heating time (1 h) on the properties of LSMO perovskite as an oxygen electrode.

Herein, a Pechini route has been successfully used to synthesize homogeneous nanometric $La_{0.5}Sr_{0.5}MnO_3$ powder with high purity. The influence of anions and cations of electrolytes such as KOH, NaOH, and K_2SO_4 and mass loading on the ORR kinetics of this perovskite was examined.

✉ Nicolas Alonso-Vante
   nicolas.alonso.vante@univ-poitiers.fr

1 IC2MP, UMR CNRS 7285, Université de Poitiers, 4 rue Michel Brunet, F-86073 Poitiers, France

2 Laboratoire d'Energétique et d'Electrochimie du Solide, Université F. Abbas Sétif-1, 19000 Sétif, Algeria

Springer

Experimental

The strontium-doped lanthanum manganite perovskite $La_{0.5}Sr_{0.5}MnO_3$ (LSMO) was synthesized following a procedure similar to that used for other metal oxide powders such as $LaMnO_3$ perovskite [9] and $LiMn_2O_4$ spinel [10]. The process involves the dissolution of nitrate salts in a mixture of a carboxylic acid, such as citric acid, and a polyol (ethylene glycol). Previous works on this process have suggested that three basic reactions, i.e., formation of metal chelates, esterification, and polymerization, occur during the formation of the polymeric precursor [11]. A clear solution was obtained by heating a mixture of citric acid and ethylene glycol (1:4 M ratio) at 90 °C for 30 min. The nitrates such as $La (NO_3)_3.6H_2O$, $Sr (NO_3)_2$, and $CH_4MnO_4.4H_2O$ (Sigma-Aldrich) were added in the appropriate amounts based on the stoichiometric ratios of $La_{0.5}Sr_{0.5}MnO_3$ (La:Sr:Mn = 0.5:0.5:1 M ratio). The resulting solution was further heated at 140 °C for 30 min to induce esterification and remove excess of ethylene glycol. The viscous solution was vacuum dried at 180 °C to yield an organic polymer precursor [12]. Black powders were obtained by heating in air the precursor, at temperatures ranging from 500 to 800 °C with an increment of 100 °C. A single-phase perovskite structure was obtained by heating samples at 700 °C during 1 h. Because the oxygen stoichiometry was not quantified, the oxide, thus, produced will be denoted hereafter by the formula $La_{0.5}Sr_{0.5}MnO_3$.

Electrode Preparation

Commercial carbon black (Vulcan XC-72, surface area of ca.250 m^2/g) was physically mixed with the perovskite and used as a support (LSMO/C) for the oxygen reduction reaction. The use of carbon black was found to improve significantly the conductivity, thus favoring the electrocatalytic activity of oxide-based electrode centers [13, 14]. Inks of the dispersed LSMO were made by mixing 1 mg LSMO powder (20 wt.%) and 4 mg of carbon (80 wt.%) with 40 μL Nafion® solution (5% in mixture of lower aliphatic alcohols and water, Aldrich) and 750 μL ultrapure water (18 MΩ cm) and 250 μL isopropanol in an ultrasonic bath for 2 h. The final concentration of LSMO in the suspension was about 1 μg/μL. In order to immobilize LSMO/carbon, a glassy carbon (GC) disk was polished with a 3A alumina slurry to get a mirror finish surface. Volumes of 0.5, 2, 3, 5, and 7 μL of the ink corresponding to the LSMO electrocatalyst loadings of 7, 27.5, 41, 68.5, and 96 $μg_{LSMO}/cm^2$ were pipetted and deposited as thin layers onto the previously polished glassy carbon surface (0.07 cm^2) of the rotating disk electrode (RDE).

Physical Characterization

The oxide structure was examined by X-ray diffraction (XRD) using a diffractometer system XPERT-PRO with a Cu-$K_{\alpha 1}$ (λ = 1.5406 Å) radiation. Phase composition identification was carried out by comparing the experimental profiles with database structures (ICSD—Inorganic Crystal Structure Database). The morphology and size of particles were examined by a JEOL JEM-2001 transmission electron microscope (operating at 200 kV) equipped with a LaB_6 filament and coupled to energy-dispersive X-ray spectroscopy (EDX). Thermogravimetric analysis and differential scanning calorimetry (TGA-DSC) were taken with an apparatus SDT Q600 (MT INSTRUMENTS), under a controlled atmosphere of argon.

Electrochemical Measurements

All electrochemical experiments were performed at room temperature (25 °C) using an Autolab Potentiostat PGSTAT 30 and a thermostated three-electrode cell. The counter electrode used was a glassy carbon with a large surface area. A reversible hydrogen electrode (RHE, 0.1 M KOH (pH 13.3), and 0.1 M NaOH (pH 13.2)) was used as the reference electrode. In 0.1 M K_2SO_4 electrolyte (pH 7.2), a Mercury-mercurous sulfate electrode (MSE: Hg/Hg_2SO_4, K_2SO_4 (0.1 M) 0.64 V vs. SHE) was employed. The applied electrode potential in this medium was also quoted with respect to the RHE using the equation (E (RHE)/V = E (MSE) + 0.059 pH + 0.64).

Before electrochemical measurements, the electrolyte was purged with nitrogen gas for 10 min. The electrode was subjected to 20 cycles between 0.05 and 1.2 V vs. RHE potential range to clean and activate the electrode surface. Linear sweep voltammetry (LSV) was performed from 1 to 0.2 V vs. RHE over a range of rotation rates of 400, 900, 1600, and 2500 rpm, at a scan rate of 5 mV s^{-1}, using a rotating disk electrode in an oxygen-saturated electrolyte solution. The electrolyte solutions were 0.1 M KOH, 0.1 M NaOH, and 0.1 M K_2SO_4.

Results and Discussion

TGA/DSC Study

Thermogravimetric analysis and differential scanning calorimetry (TGA-DSC) curves of the polymeric precursor are shown in Fig. 1. The total weight loss was 6 mg from room temperature to 900 °C. The first weight loss estimated to 7% in the temperature range 22–200 °C can be attributed to evaporation of water from LSMO. The second weight loss of 65% in the temperature range 200–350 °C is assigned to evaporation of ethylene glycol, decomposition of citric acid, and evaporation of structurally bounded water. The third step in the
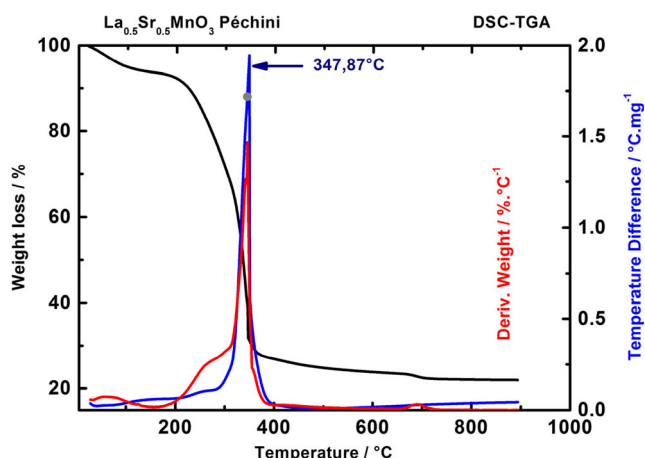
Fig. 1 TGA-DSC curves of La$_{0.5}$Sr$_{0.5}$MnO$_3$ (LSMO) perovskite gel precursor synthesized by Pechini method and dried at 200 °C

process, ranging from 350 to 700 °C, with 5% weight loss can be explained by decomposition of the metal citrate complex and combustion of the residual organics. This behavior was found to be typical for the pyrolysis of certain citrate precursors [15]. The peaks, located at about 350 °C, are exothermic on the DSC curve due to decomposition of nitrates and organic matter and correspond to the second weight loss as detected in the TGA curve. The decomposition of all nitrates and citrates occurred below 500 °C, leading to the formation of the oxide powder. It can be inferred from these data that the final product can only be obtained by annealing at temperature equal to or higher than 700 °C.

XRD Characterization

Figure 2 shows some selected XRD patterns at 500, 600, and 700 °C obtained after in situ heat treating the gel precursor from room temperature to 700 °C. Scans were recorded at 0.06°/s for 2θ values between 12° and 80° at a heating rate of 10 °C/min. The results indicate that the formation of a perovskite phase started from 600 °C. No shift in the diffraction peaks can be observed for the sample, and all the peaks can be well indexed to a pure perovskite with a tetragonal crystal structure (space group I4/mcm, a = 5.4425 Å, b = 5.4425 Å, and c = 7.7661 Å) according to the PDF ICSD N° 01-089-0786. The average crystallite size (D) was determined using the Debye-Scherrer equation [16]:

$$D = \frac{0.9\lambda}{H_K \cos\theta} \quad (1)$$

where D is the average crystallite size (Å) in the direction hkl, H_k the full-width at half-maximum (FWHM) in radian, θ the Bragg angle in degrees, and λ the incident X-ray wave length (λ_{Cu} = 1.5418 Å).

The average crystallite sizes (D) of the LSMO sample calcined for 1 h at 600, 700, and 800 °C were 12, 15.8, and
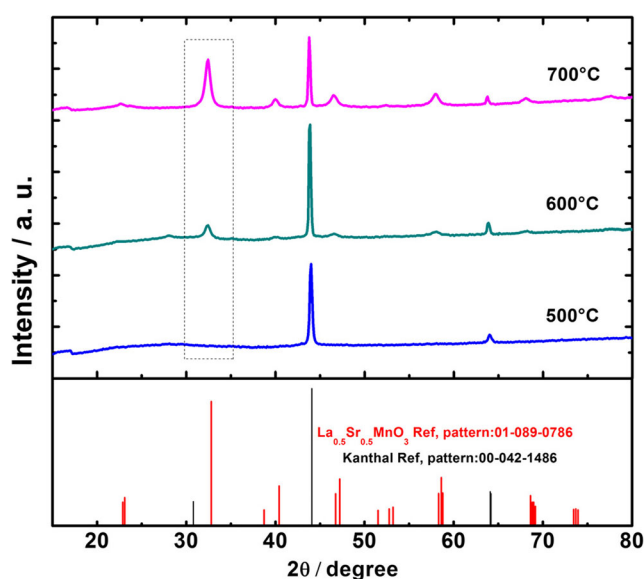

Fig. 2 XRD patterns of LSMO oxide heat treated at different temperatures. The *dashed frame* shows the evolution with the heat-treatment temperature of peak (112)

16.4 nm, respectively. This result confirms that the primary particles of the LSMO powders prepared by the Pechini method in the present work are nanosized perovskite phase materials and indicates that the grains' size increases with the increasing heat-treatment temperature. The two peaks appearing at 44° and 64° on all the diffractograms are attributed to the support Kanthal (FeCrAl alloy) according to the PDF N° 00-042-1486.

Morphology

TEM images of LSMO powders heat-treated at different temperatures are shown in Fig. 3. The images show that all samples are nanoparticulated (sphere-like) practically identical, including quality, shape, and size, with regions showing a roughly agglomeration. The sizes of these nanoparticles (between 12 and 15 nm) are in good agreement with those obtained by the XRD diffraction patterns. The elemental energy-dispersive X-ray (EDX) spectrum in Fig. 3d shows the presence of La, Mn, Sr, and O elements of the sample heat treated at 700 °C for 1 h and their relative abundance in the L$_{0.5}$Sr$_{0.5}$MnO$_3$ perovskite. The EDX of the particles indicated a homogenous distribution of La, Mn, Sr, and O elements.

Electrochemical Characterization of LSMO/C Electrocatalyst

The ORR catalytic activity of (LSMO/C) heat-treated at different temperatures was measured by RDE depositing the samples with the same loading (68.5 μg$_{LSMO}$/cm^2) on a glassy carbon (GC) electrode disk in O$_2$-saturated 0.1 M

Fig. 3 TEM images of heat-treated LSMO: **a** 500 °C, **b** 600 °C, **c** 700 °C for 1 h, and **d** EDX spectrum of LSMO heat treated at 700 °C for 1 h
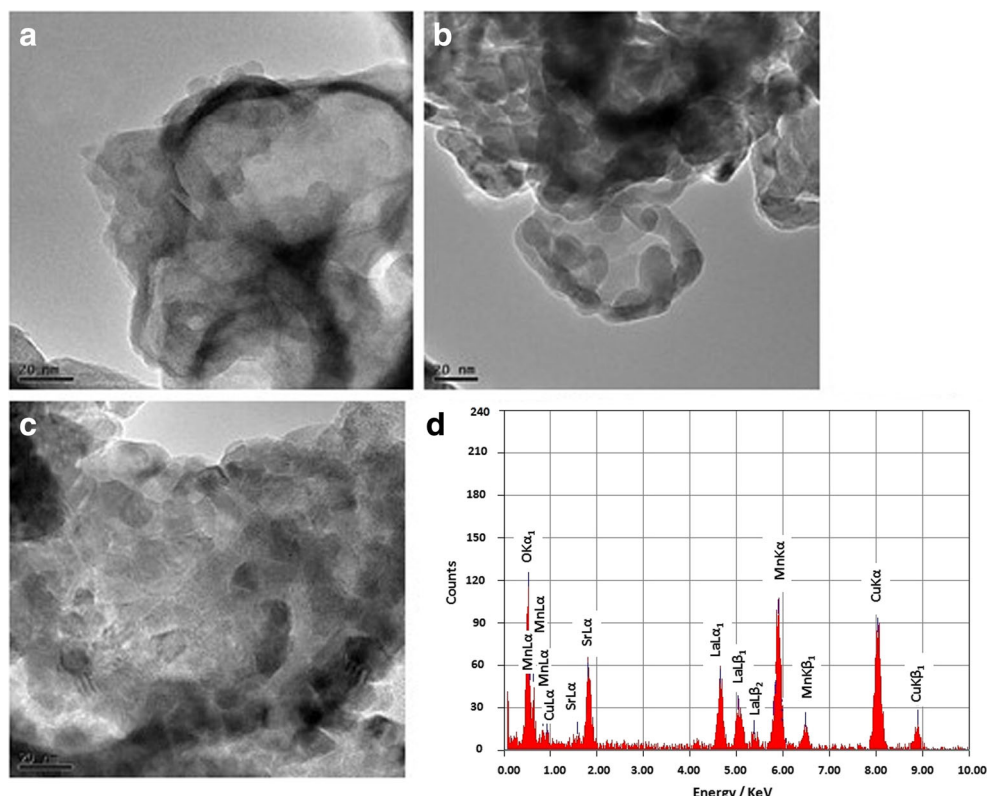
KOH electrolyte. Regardless of the heat treatment temperature, the LSV curves display a mixed kinetic diffusion-controlled region at high potentials and a diffusion-limiting current (j_{lim}) region at low potentials, see Fig. 4. The comparison between LSV curves indicates that the LSMO/C electrode heat-treated at 700 °C showed the highest catalytic activity with a concomitant half-wave potential ($E_{1/2}$) shifted to more positive potential and
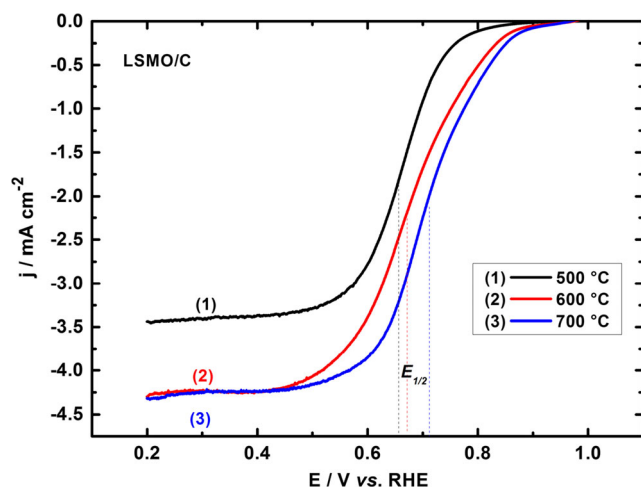
higher limiting current density, j_{lim}, than those heat treated at 500 and 600 °C. This phenomenon, apparently, puts in evidence the crystalline state of the sample [17]. Therefore, heat treatment at this temperature was selected for further experiments. The LSV curve of LSMO heat treated at 500 °C provided the highest surface area, but exhibited a poor catalytic activity with the lowest half-wave potential.

To understand whether this activity is attributed to the nanocrystalline state of the sample, the electrochemically active area was measured, as described in reference [18], for the three samples by evaluating the oxide roughness factor (RF), i.e., the ratio of the real area (S_{LMSO}) of a rough electrode to its geometrical one. The capacitive current density, j_{cap}, was determined as a function of the scan rate (30 to 80 mV s^{-1}) by recording cyclic voltammograms for all three heat-treated samples (500, 600, 700 °C) in a small potential region of 100 mV (i.e., 0.35 to 0.45 V). A typical example is depicted in the inset of Fig. 5. The double-layer capacitance (C_{dl}) was estimated from the slope of Fig. 5. The roughness factor (RF) was then calculated by assuming a double-layer capacitance of 60 μF cm^{-2} for a smooth oxide surface [19]. Values of C_{dl} and RF for the three samples are summarized in Table 1.

From the table, RF specifies that LSMO oxide calcined at 500 °C has the highest electrochemically surface area than those calcined at 600 and 700 °C. Although the surface area value of LSMO/C/500 °C appears to be the highest, it revealed
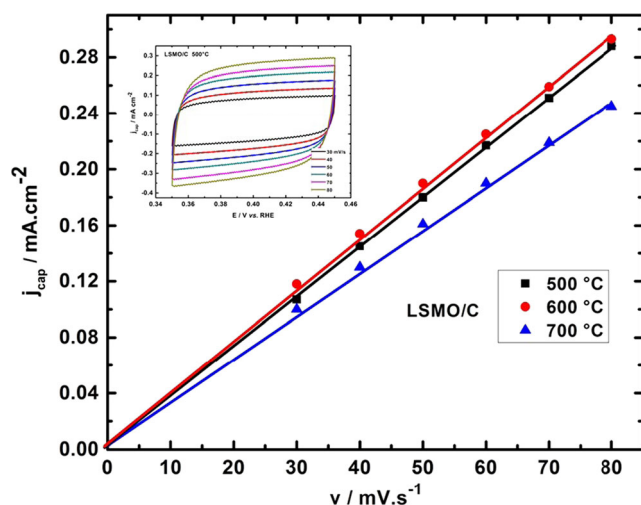
Fig. 4 LSV curves for ORR of LSMO calcined at (*1*) 500 °C, (*2*) 600 °C, and (*3*) 700 °C, in O$_2$-saturated 0.1 M KOH solution at 900 rpm. Scan rate at 5 mV s^{-1} and 25 °C

Fig. 5 Plots of capacity current j_{cap} (estimated at 0.43 V) vs. scan rate for electrocatalysts calcined at 500, 600, and 700 °C, in OH 0.1 M, insert is typical cyclic voltammograms for the LSMO/C electrode calcined at 500 °C

the poorest electrocatalytic activity, suggesting that ORR process on LSMO/C is, therefore, assigned to the degree of crystallinity rather than to the surface area. To assess the effect of carbon Vulcan on the electroactivity of the LSMO perovskite, LSV voltammograms of the carbon-supported perovskite were compared to those non-supported perovskite, Fig. 6a, CVs at 50 mV/s for carbon Vulcan, LSMO/C and LSMO, see Fig. 6b. It can be observed, according to cyclic voltammograms for carbon in O_2 and N_2 saturated 0.1 M KOH, respectively, that carbon actively contributes in the ORR on LSMO/C composites. Composite electrodes as LSMO/C activate the ORR via four-electron pathway whereas carbon alone is only able to catalyze the two-electron one [14]. It comes up clearly that using Vulcan carbon as a support for LMSO improves the charge transfer of nanoparticulated LSMO at overpotential beyond the activation region, as compared to non-supported LSMO, which shows kinetic hindrance in agreement with the literature [20, 21]. Within the ORR-recorded potential interval, we can qualitatively evaluate the $E_{1/2}$ and j_{lim} increase in the order CV < LSMO < LSMO/C. Compared to other studies from the literature on supported and non-supported similar perovskites, LSMO/C electrocatalyst provides an ORR-limiting current density of 4 vs. 2.2 mA cm^{-2} at 0.4 V vs. RHE [14], and 4 vs.1.25 mA cm^{-2} at 0.2 V [7].

Effect of the Electrolyte

To examine whether the cations K$^+$ and Na$^+$ and the anion SO_4^{2-} influence the ORR activity on the LSMO oxide surface, a set of LSVs was plotted at 5 mVs^{-1} for the electrocatalyst loaded with 68.5 $\mu g_{LSMO}/cm^2$ in O_2-saturated 0.1 M solutions of KOH, NaOH, and neutral K_2SO_4, see Fig. 7. The shape of the current-potential curves is similar for all electrolytes. Their analysis shows that the half-wave potential, $E_{1/2}$, and the kinetic current density, j_k, increase following this order K_2SO_4 < NaOH < KOH. Taking into consideration the roughness factor (RF) of each sample, the values of the real ORR kinetic current density obtained at 0.7 V (see insert in Fig. 7) in KOH, NaOH, and K_2SO_4 electrolytes were found to be 96.7, 49.3, and 14.3 $\mu A/cm^2_{LMSO}$, respectively, indicating that KOH solution is a superior medium for ORR under both thermodynamic and kinetic considerations in agreement with the literature [22]. However, the high improvement of ORR activity on Pt electrode was assigned to the high oxygen solubility and diffusivity and lower viscosity of the solution by Jin et al. [23]. The oxygen diffusivity is related to the viscosity, η, of the electrolyte, and the diffusion coefficient D_{O2} is given by the Stokes-Einstein equation [24]:

$$D_{O_2} = \frac{k_B T}{(6\pi r \eta)} \tag{2}$$

where r is the effective hydrodynamic radius of the oxygen molecule, k_B is the Boltzmann constant, and T is the absolute temperature. As the viscosity of NaOH electrolyte is higher than that of KOH [23], the D_{O2} in NaOH is lower than that in KOH; thus, a smaller limiting current density j_{lim} is expected, according to Levich equation [25]. Furthermore, because Na$^+$ ion is smaller in size and higher in charge density than the K$^+$ ion, the salting-out effect, based on the electrolyte-oxygen interaction, is stronger in NaOH than that in KOH [26], leading to the inhibition of oxygen dissolution and, consequently, to a smaller limiting current density in NaOH solution as seen in Fig. 7. Suntivich et al. [27] and Strmcnik et al. [28] proposed that the non-covalent interaction between cations (K$^+$, Na$^+$) and the oxide does not lead to the blockage of ORR active sites, but rather to the modification of the reaction intermediate energy. In the case of K$^+$ which has the weakest interaction
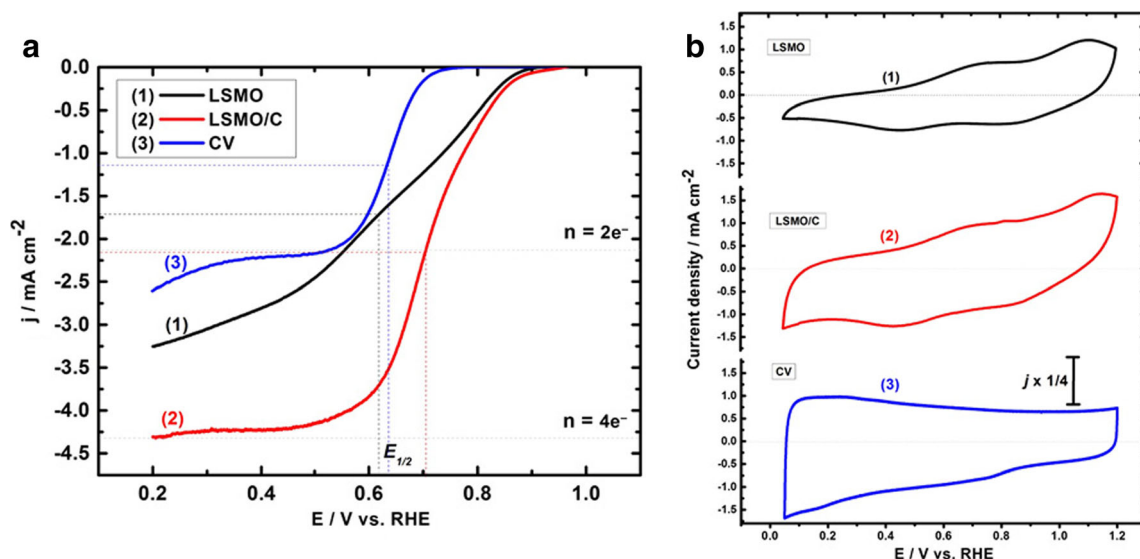
Table 1 Values of C_{dl} and roughness factor (RF) and ORR kinetic current density at 0.7 V vs. RHE in 0.1 M KOH for LSMO samples calcined at different temperatures

Heat-treated LSMO sample	C_{dl} ($\mu F/cm^2$)	RF	j_k mA/cm$^2_{geo}$	j_k $\mu A/cm^2_{LSMO}$
700 °C	2880	48	5	104
600 °C	3480	58	3	51
500 °C	3600	60	1.028	21

Fig. 6 a LSV curves for ORR of (*1*) LSMO, (*2*) LSMO/C, and (*3*) carbon Vulcan in O_2-saturated 0.1 M KOH solution at 900 rpm. Scan rate 5 mV s^{-1} and 25 °C. Calculated limiting current from Levich equation for two and four electrons are indicated, as well as the half-wave potential for each curve. **b** The corresponding CVs of (*1*) LSMO, (*2*) LSMO/C, and (*3*) carbon Vulcan in N_2-saturated 0.1 M KOH solution at scan rate 50 mV s^{-1} and 25 °C

with the OH_{ad}, the modification is minimal, and thus, the ORR proceeds as if the cation was not present. In the case of sulfate anions SO_4^{2-}, the ORR overpotential losses and the electroactivity increased. In general, the presence of strongly adsorbed anions in the electrolytes such as H_2SO_4, H_3PO_4 results in the appearance of high overpotentials for the ORR on Pt cathode. This effect is not observed, however, when the ORR is evaluated in non-adsorbing (negligible) electrolytes such as $HClO_4$ or

alkaline electrolytes [29]. For instance, poorer performance of Pt cathodes for the ORR in concentrated H_3PO_4 than in KOH may be attributed to limitations arising from adsorption of phosphoric acid anions [30]. According to Dominguez et al. [31], the observed negative effect of sulfates for the ORR on both Fe/N/C and Fe/N/CNT composites in 0.5 H_2SO_4 is due to both the removal of acid-soluble Fe species and the presence of sulfates onto the active sites. These anions remain bonded to the active sites rather than simply blocking the access of O_2 into the active sites.
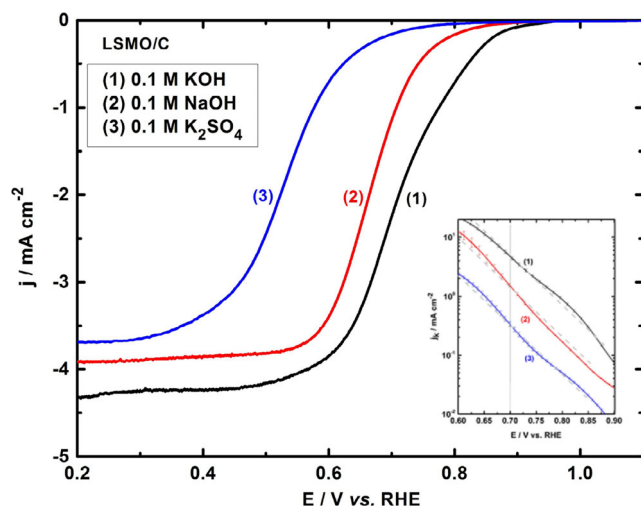
Effect of the LSMO Loading

In order to investigate the optimal amount of LSMO in the LSMO/C for best ORR activity, LSMO/C electrocatalysts with various mass loadings of the LSMO oxide, heat-treated at 700 °C, were studied and evaluated. Figure 8 represents LSVs obtained on the LSMO/C electrodes in 0.1 M KOH under the same conditions, that is, oxygen-saturated electrolyte, 25 °C, and an angular velocity ω of the RDE of 900 rpm. To compare the electrocatalytic activity of LSMO/C electrodes with that of benchmark materials, such as Pt/Vulcan [32], a commercial Pt/C (20 wt.% Pt on carbon, Johnson-Matthey) was also tested under the same conditions. In the studied interval of catalyst mass loadings, it is observed that the higher the mass loading added of LSMO/C, the higher the half-wave potential and the limiting and kinetic current densities. Within the experimental error, mass loadings of LSMO/C of 68.5 μg$_{LSMO}$/cm^2 and that of 96 μg$_{LSMO}$/cm^2 delivered the same results, demonstrating that this mass loading between 70 and 90 μg$_{LSMO}$/cm^2 can be considered as an

Fig. 7 ORR current-potential curves on LSMO/C calcined at 700 °C, recorded at 900 rpm, 5 mV s^{-1} and 25 °C in O_2-saturated; (*1*) 0.1 M KOH (pH 13.35), (*2*) 0.1 M NaOH (pH 13.25), and (*3*) 0.1 M K_2SO_4 (pH 7.2) electrolytes. Insert: Tafel plot of the corrected mass transfer RDE characteristics
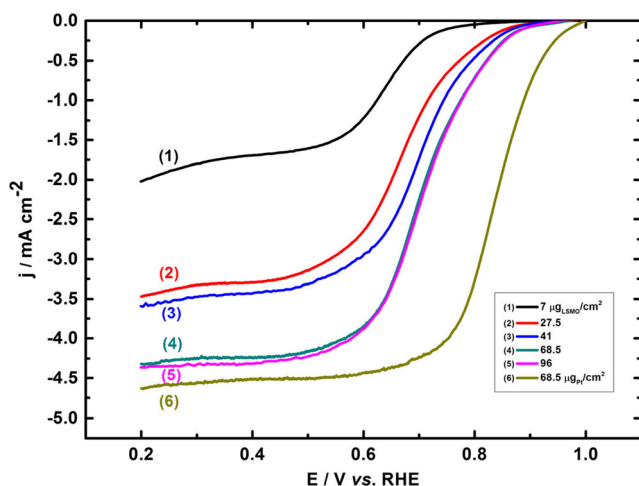
Fig. 8 ORR current-potential characteristics on different mass loadings of LSMO/C at 900 rpm in a 0.1 M KOH O_2-saturated solution. Scan rate at 5 mV s^{-1} and 25 °C

optimum for ORR in alkaline fuel cells. However, under the same condition, this mass loading remains less electroactive than the Pt/C electrocatalyst.

For better comparison, the dependence of the ORR half-wave potential (E$_{1/2}$) and the limiting current density, j_{lim}, on LSMO and Pt deposited loadings is contrasted in Fig. 9. It is clearly observed that, for both electrocatalysts, as the loading increases the E$_{1/2}$ of the ORR at first increases and reaches a plateau, and the j_{lim} significantly develops up to 41 µg$_{LSMO}$/cm^2 and after remains almost constant. Furthermore, the half-wave potentials of Pt/C electrocatalyst are considerably more positive than those of the LSMO/C one, and the limiting current densities of the Pt/C are slightly larger than those corresponding to the LSMO/C, indicating that the LSMO/C electroactivity towards the ORR in 0.1 M KOH approaches that of the Pt/C one.
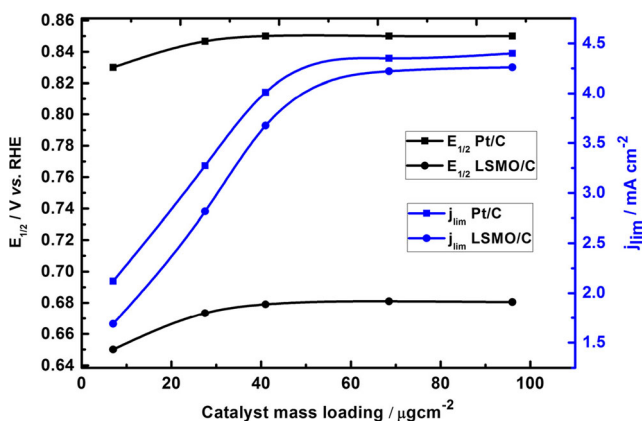

Fig. 9 ORR half-wave potential and limiting current density (at 0.4 V vs. RHE) for the LSMO/C and Pt/C electrodes vs. the LSMO and Pt mass loadings in O_2-saturated 0.1 M KOH solution at 900 rpm and 5 mVs^{-1}. *Circles* and *square* symbols represent the E$_{1/2}$ and j_{lim} for the LSMO/C and Pt/C, respectively

The active surfaces of the various sample loadings were estimated by evaluating the LSMO roughness factors which were found to be 39, 45, and 48 for LSMO loadings 27.5, 41, and 68.5 µg$_{LSMO}$/cm^2, respectively. As expected, the RF increases with increasing LSMO loading. Based on the results provided by the LSV and capacitive curves, it should be pointed out that the ORR activity depends intimately on the catalytic site density. The influence of catalytic loading on the ORR activity was recently reported on precious and non-precious metal centers, such as Pt/C [33], CoSe$_2$/C in acid [34], and alkaline media [35]. It should be mentioned that an increase of catalyst depositing volume from 0.5 to 7 µL suggests the higher thickness of LSMO/C film which reflects the higher number of site density. As discussed previously in detail [36], the activity of the catalyst is directly related to the site density.

To examine the pathway for the ORR via two or four electrons, LSV curves at various rotation speeds ω were plotted. Figure 10a, given as an example, shows for LSMO/C loaded with a mass of 68.5 µg$_{LSMO}$/cm^2 calcined at 700 °C that the limiting current density increases with increasing ω due to the improved mass transport of oxygen at the electrode surface. This series of experiments assesses the idea that the ORR process is essentially being done via a series process, whatever the nature of the catalytic center, as demonstrated herein with LSMO perovskites, on LaCoO$_3$ [37], and other kinds of electrode materials [34–36].

The desired feature of a good catalyst towards the ORR would be to reduce molecular oxygen to OH^- through the direct four-electron process [38]. A two-electron reduction of O_2 via HO_2^- peroxide [39] leads to a lower energy conversion efficiency. In order to verify the ORR pathway, Koutecky-Levich (K-L) plots corresponding to the LSV curves of Fig. 10a are plotted in Fig. 10b using the Koutecky-Levich (K-L) equation [25]:

$$\frac{1}{j} = \frac{1}{j_k} + \frac{1}{j_{lim}} = \frac{1}{j_k} + \frac{1}{B\omega^{1/2}} \tag{3}$$

$$B = 0.62nFAC_{O_2}D_{O_2}^{2/3}\nu^{-1/6} \tag{4}$$

where j, j_k, and j_{lim} are the measured disk current density, kinetic current density, and diffusion-limiting current density, respectively, and ω is the electrode rotation rate (rad s^{-1}). Furthermore, n is the number of electrons in the ORR, F is the Faraday constant (96,500 C mol^{-1}), A is the area of the disk electrode (0.07 cm^2), C_{O_2} is the oxygen concentration in 0.1 M KOH (1.14 × 10^{-6} mol cm^{-3}), D_{O_2} is the oxygen diffusion coefficient in 0.1 M KOH (1.73 10^{-5} cm^2 s^{-1}), and ν is the kinematic viscosity of the 0.1 M KOH solution (0.01 cm^2 s^{-1}). All plots in Fig. 10b determine linear and parallel relationship with j_{lim}^{-1} as function of $\omega^{-1/2}$ at four
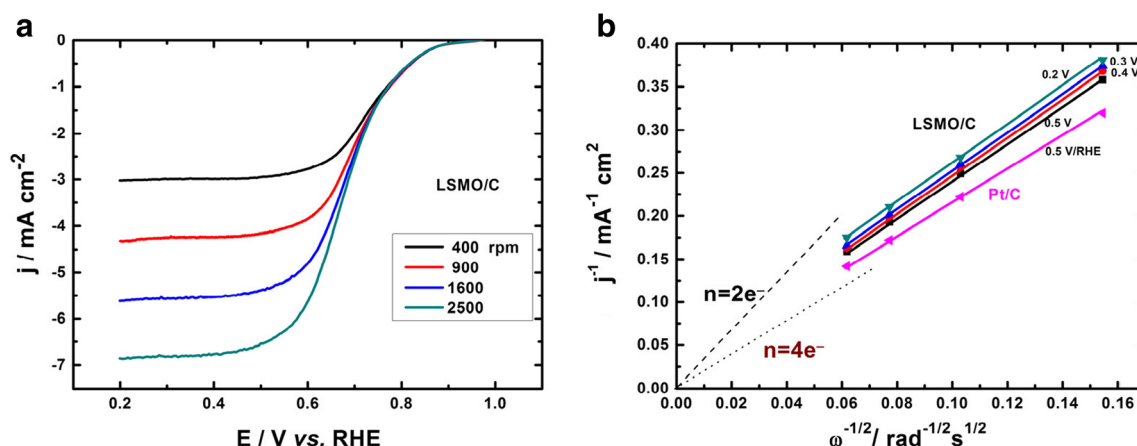
Fig. 10 **a** ORR current-potential curves on LSMO/C at different rotation rates in a 0.1 M KOH O_2-saturated solution at 5 mV s^{-1} and 25 °C. **b** Koutecky-Levich plots (including that of Pt/C composite) at different selected applied electrode potentials; *dotted lines* represent theoretical current values for two and four electrons

selected applied electrode potentials, implying therefore consistent diffusional characteristics of ORR kinetics on the LSMO/C electrocatalyst. From the slopes, B of the K-L plots (Fig. 10b), calculation of the number of electrons transferred per O_2 provides, as for as Pt/C composite, four electrons for LSMO/C.

Conclusion

This study was carried out to evaluate the activity of the perovskite $La_{0.5}Sr_{0.5}MnO_3$/C used as an electrocatalyst for the oxygen reduction reaction (ORR). The ORR on the LSMO/C electrocatalyst surface was studied using voltammetry techniques and the influence of heat treatment temperature. The mass loading and the nature of electrolyte were also examined. The results obtained allowed the following conclusions:

(i) The Pechini method was successfully used at low temperature to produce $La_{0.5}Sr_{0.5}MnO_3$ homogeneous nanometric-sized material with high purity.

(ii) The LSMO calcined at 700 °C for 1 h showed higher electroactivity in 0.1 KOH with a higher half-wave potential than its counterparts heat-treated at 500 and 600 °C.

(iii) The performance for ORR of the LSMO/C electrocatalyst in different electrolytes, e.g., KOH, NaOH, and K_2SO_4, was examined. Higher ORR electroactivity has been observed in KOH electrolyte as compared to NaOH and K_2SO_4 ones.

(iv) The higher the LSMO loading added to the LSMO/C composite, the higher is the ORR electroactivity. The LSMO/C with higher loadings exhibited an encouraging electrocatalytic activity, approaching that of the more expensive fuel cell Pt/C cathode examined under the same conditions.

(v) By examining Koutecky-Levich plots, the ORR materials' activity is apparently due to four-electron charge transfer. This is the result of increasing the number of accessible active sites with the mass loading.

References

1. K. Gong, F. Du, Z. Xia, M. Durstock, L. Dai, Science **323**, 760 (2009)
2. E.M. Garcia, H.A. Tarôco, T. Matencio, R.Z. Domingues, J.A. dos Santos, Int. J. Hydrog. Energy **37**, 6400 (2012)
3. J. Suntivich, H.A. Gasteiger, N. Yabuuchi, H. Nakanishi, J.B. Goodenough, Y. Shao-Horn, Nat. Chem. **3**, 546 (2011)
4. D. Geng, Y. Chen, Y. Chen, Y. Li, R. Li, X. Sun, S. Ye, S. Knights, Energy Environ. Sci. **4**, 760 (2011)
5. C. Jin, X. Cao, L. Zhang, C. Zhang, R. Yang, J. Power Sources **241**, 225 (2013)
6. C. Zhu, A. Nobuta, I. Nakatsugawa, T. Akiyama, Int. J. Hydrog. Energy **38**, 13238 (2013)
7. J. Tulloch, S.W. Donne, J. Power Sources **188**, 359 (2009)
8. E. Siebert, A. Hammouche, M. Kleitz, Electrochim. Acta **40**, 1741 (1995)
9. P.A. Lessing, Am. Ceram. Soc. Bull. **68**, 1002 (1989)
10. W. Liu, G.C. Farrington, F. Chaput, B. Dunn, J. Electrochem. Soc. **143**, 879 (1996)
11. S.C. Zhang, G.L. Messing, W. Huebner, M.M. Coleman, J. Mater. Res. **5**, 1806 (1990)
12. M. Pechini, US Patent 3.330.697 (1967)
13. D. Thiele, A. Züttel, J. Power Sources **183**, 590 (2008)
14. T. Poux, F.S. Napolskiy, T. Dintzer, G. Kéranguéven, S.Y. Istomin, G.A. Tsirlina, E.V. Antipov, E.R. Savinova, Catal. Today **189**, 83 (2012)
15. M.S.G. Baythoun, F.R. Sale, J. Mater. Sci. **17**, 2757 (1982)
16. B.D. Cullity, *Answers to Problems: Elements of X-Ray Diffraction* (Wesley Publishing Company, Addison, 1978)
17. W.S. Kim, G. Anoop, H.J. Lee, S.S. Lee, J.H. Kwak, H.J. Lee, J.Y. Jo, J. Catal. **344**, 578 (2016)

18. S.K. Tiwari, P. Chartier, R.N. Singh, J. Electrochem. Soc. **142**, 148 (1995)
19. S. Levine, A.L. Smith, Discuss. Faraday Soc. **52**, 290 (1971)
20. G. Kéranguéven, S. Royer, E. Savinova, Electrochem. Commun. **50**, 28 (2015)
21. M. Bursell, M. Pirjamali, Y. Kiros, Electrochim. Acta **47**, 1651 (2002)
22. D. Strmcnik, D.F. van der Vliet, K.-C. Chang, V. Komanicky, K. Kodama, H. You, V.R. Stamenkovic, N.M. Marković, J. Phys. Chem. Lett. **2**, 2733 (2011)
23. W. Jin, H. Du, S. Zheng, H. Xu, Y. Zhang, J. Phys. Chem. B **114**, 6542 (2010)
24. J.C. Li, P. Chang, J. Chem. Phys. **23**, 518 (1955)
25. A.J. Bard, L.R. Faulkner, J. Leddy, C.G. Zoski, *Electrochemical Methods: Fundamentals and Applications* (Wiley, New York, 1980)
26. M. Görgényi, J. Dewulf, H. Van Langenhove, K. Héberger, Chemosphere **65**, 802 (2006)
27. J. Suntivich, E.E. Perry, H.A. Gasteiger, Y. Shao-Horn, Electrocatalysis **4**, 49 (2013)
28. D. Strmcnik, K. Kodama, D. van der Vliet, J. Greeley, V.R. Stamenkovic, N.M. Marković, Nat. Chem. **1**, 466 (2009)
29. K.L. Hsueh, E.R. Gonzalez, S. Srinivasan, Electrochim. Acta **28**, 691 (1983)
30. K.F. Blurton, E. McMullin, Energy Convers. **9**, 141 (1969)
31. C. Domínguez, F.J. Pérez-Alonso, J.L. Gómez de la Fuente, S.A. Al-Thabaiti, S.N. Basahel, A.O. Alyoubi, A.A. Alshehri, M.A. Peña, S. Rojas, J. Power Sources **271**, 87 (2014)
32. S. Taylor, E. Fabbri, P. Levecque, T.J. Schmidt, O. Conrad, Electrocatalysis **7**, 287 (2016)
33. L. Timperman, Y.J. Feng, W. Vogel, N. Alonso-Vante, Electrochim. Acta **55**, 7558 (2010)
34. Y. Feng, T. He, N. Alonso-Vante, Electrochim. Acta **54**, 5252 (2009)
35. Y. Feng, T. He, N. Alonso-Vante, Chem. Mater. **20**, 26 (2008)
36. N. Alonso-Vante, ChemPhysChem **11**, 2732 (2010)
37. T. Poux, A. Bonnefont, A. Ryabova, G. Kerangueven, G.A. Tsirlina, E.R. Savinova, Phys. Chem. Chem. Phys. **16**, 13595 (2014)
38. L. Demarconnay, C. Coutanceau, J.-M. Léger, Electrochim. Acta **49**, 4513 (2004)
39. E. Yeager, J. Mol. Catal. **38**, 5 (1986)